

Evaluation of spin diffusion length and spin Hall angle of antiferromagnetic Weyl semimetal Mn_3Sn .

P. K. Muduli^{1,*}, T. Higo¹, T. Nishikawa¹, D. Qu¹, H. Isshiki¹, K.

Kondou², D. Nishio-Hamane¹, S. Nakatsuji¹, and YoshiChika Otani^{1,2†}

¹*Institute for Solid State Physics, University of Tokyo, Kashiwa 277-8581, Japan and*

²*Center for Emergent Matter Science, RIKEN, 2-1 Hirosawa, Wako 351-0198, Japan*
(Dated: February 19, 2019)

Antiferromagnetic Weyl semimetal Mn_3Sn has shown to generate strong intrinsic anomalous Hall effect (AHE) at room temperature, due to large momentum-space Berry curvature from the time-reversal symmetry breaking electronic bands of the Kagome planes. This prompts us to investigate intrinsic spin Hall effect, a transverse phenomenon with identical origin as the intrinsic AHE. We report inverse spin Hall effect experiments in *nanocrystalline* Mn_3Sn nanowires at room temperature using spin absorption method which enables us to quantitatively derive both the spin diffusion length and the spin Hall angle in the same device. We observed clear absorption of the spin current in the Mn_3Sn nanowires when kept in contact with the spin transport channel of a lateral spin-valve device. We estimate spin diffusion length $\lambda_{s(\text{Mn}_3\text{Sn})} \sim 0.75 \pm 0.67$ nm from the comparison of spin signal of an identical reference lateral spin valve without Mn_3Sn nanowire. From inverse spin Hall measurements, we evaluate spin Hall angle $\theta_{SH} \sim 5.3 \pm 2.4$ % and spin Hall conductivity $\sigma_{SH} \sim 46.9 \pm 3.4$ (\hbar/e) ($\Omega \text{ cm}$)⁻¹. The estimated spin Hall conductivity agrees with both in sign and magnitude to the theoretically predicted intrinsic $\sigma_{SH}^{int} \sim 36\text{-}96$ (\hbar/e) ($\Omega \text{ cm}$)⁻¹. We also observed anomalous Hall effect at room temperature in nano-Hall bars prepared at the same time as the spin Hall devices. Large anomalous Hall conductivity along with adequate spin Hall conductivity makes Mn_3Sn a promising material for ultrafast and ultrahigh-density spintronics devices.

PACS numbers: xx.xx

I. INTRODUCTION

Next generation of ultra-fast and ultra-low-power spintronic devices will be ideally mass-less and dissipation-less. Therefore, antiferromagnetic materials with topological properties are most desirable for future spintronics devices. Antiferromagnetic materials are expected to overtake ferromagnetic materials in future spintronics devices due to their higher intrinsic excitation frequency in terahertz (THz) timescale, immunity against external field perturbations and zero net magnetization [1, 2]. Many antiferromagnetic materials have recently been found to exhibit either topologically protected massless Dirac or Weyl quasiparticles in their band structure or topologically non-trivial real-space spin textures. These exotic antiferromagnets have led to a new area of research called *topological antiferromagnetic spintronics* [3]. So far two antiferromagnets CuMnAs and Mn_2Au exhibiting current-induced Néel spin-orbit torque are the prime materials in antiferromagnetic spintronics which have already led to working devices [4–6]. Over the past years many other antiferromagnets like SrMnBi_2 [7], EuMnBi_2 [8], BaFe_2As_2 [9], YbMnBi_2 [10], GdPtBi [11, 12], FeSe [13], NdSb [14], $\text{Eu}_2\text{Ir}_2\text{O}_7$ [15], etc., have emerged which may enrich topological antiferromagnetic spintronics further. Noncollinear antiferromagnet Mn_3X ($X = \text{Ge}, \text{Sn}, \text{Ga}, \text{Ir}, \text{Rh}$ and Pt) series have been

attracting considerable interest lately due to accidental discovery of the large anomalous Hall effect (AHE) comparable in magnitude to that of ferromagnets [16–20]. Usually AHE is not realized in ordinary collinear antiferromagnets, however, recent theoretical and experimental investigations in chiral antiferromagnets reveal that a large AHE is possible for non-vanishing Berry phase which acts as a fictitious magnetic field in momentum space [16, 21].

Here we focus particularly on Mn_3Sn which involve both Weyl physics [22, 23] and antiferromagnetism with large Néel temperature of $T_N \sim 420$ K [24]. In Mn_3Sn magneto-geometrical frustration in the Kagome lattice leads to non-collinear antiferromagnetic order causing Mn moments to lie in the *ab*-plane (Kagome-plane) with moments aligned at 120° with each other. This inverse triangular spin structure carries a very small net ferromagnetic moment of $\sim 0.002 \mu_B/\text{Mn}$ atom, 1000 times smaller than ferromagnets[25]. The triangular spins can be rotated inside the *ab*-plane even with a very weak magnetic field due to small Kagome-plane magnetic anisotropy[26]. Large anomalous Hall conductivity up to $\sigma_{xy}^{AHE} \approx 120$ ($\Omega \text{ cm}$)⁻¹ has been observed in Mn_3Sn which matches closely to the theoretically calculated σ_{xy}^{AHE} from the integration of Berry curvature over the Brillouin zone[17, 27]. Ab-initio band structure calculations [22, 23] and angle-resolved photoemission spectroscopy (ARPES) measurements [28] have revealed multiple type-2 Weyl points in the bulk band structure of Mn_3Sn . Fermi level has been found to be as close as ~ 5 meV to the nearest Weyl node with slightly extra Mn doping in Mn_3Sn [28]. Signatures of chiral anomaly

*Electronic address: muduli.ps@gmail.com

†Electronic address: yotani@issp.u-tokyo.ac.jp

such as negative longitudinal magnetoresistance and planar Hall effect has also been observed in Mn_3Sn [28]. Large thermal Hall[29], anomalous Nernst effect [29–31], topological Hall effect[32] and exotic magneto-optical Kerr effect[33] has also been detected in Mn_3Sn . Although initial studies on Mn_3Sn was primarily focused on bulk single crystals, recently, high quality thin films of Mn_3Sn showing the exchange-bias effect [34] and large anomalous Hall effect [35, 36] have been successfully fabricated and open up possibility for spintronics device applications.

Spin Hall effect and anomalous Hall effect are analogues phenomena both originating from the electronic and magnetic structure of the material. The intrinsic SHE is explained by the spin Berry curvature which is obtained from Kubo formula, similar to the AHE [37–40]. Therefore, chiral antiferromagnets are most promising materials for detecting large spin Hall effect [27, 41–43]. In direct spin Hall effect (DSHE) a charge current gives rise to a transverse spin current which generates spin accumulations with opposite spin polarization at the reverse sides of a material. Furthermore, a spin current can also induce a transverse charge current (voltage drop), in the reciprocal process called the inverse spin Hall effect (ISHE). The spin-to-charge current interconversion can be described by, $\vec{J}_S = \frac{e}{\hbar}\theta_{SH}(\vec{J}_C \times \vec{s})$, where $\vec{J}_{S(C)}$ is the spin(charge) current, \hbar is the reduced Planck's constant, e is the electronic charge and \vec{s} denotes the direction of spin polarization. The conversion efficiency is characterized by the spin Hall angle, θ_{SH} . Estimation of spin transport parameters like spin diffusion length (λ_s), spin Hall angle (θ_{SH}) and spin Hall conductivity (σ_{SH}) is indispensable for possible application of Mn_3Sn in spin-orbitronics. Very recently, a strong SHE was experimentally discovered in another chiral antiferromagnetic compound IrMn_3 and the spin Hall angle up to $\sim 35\%$ was observed [44]. Theoretical calculations suggest spin Hall effect in Mn_3Sn is strongly anisotropic and is maximized when charge current \vec{J}_C and spin current \vec{J}_S are inside the Kagome-plane[42]. Recently, Železný *et al.*[45] have predicted that spin current in noncollinear antiferromagnets possess spin components both longitudinal and transverse to the antiferromagnetic order parameter. Interestingly, these spin currents are odd under time reversal in contrast to spin Hall effect spin currents which are even. It is also expected that the transversal contribution of spin currents in noncollinear antiferromagnets can be greater than the spin Hall effect spin currents. These unconventional spin Hall effects in noncollinear antiferromagnets may open up new avenues in the understanding of spin Hall effect in antiferromagnets [43, 46].

In this paper we use spin absorption in lateral spin valves to study inverse spin Hall effect in nanocrystalline Mn_3Sn nanowires. The spin absorption method allows us to extract the spin diffusion length (λ_s) and spin Hall angle (θ_{SH}) in the same device by changing measurement configuration. In these measurements the antiferromag-

netic material is not in direct contact with the ferromagnetic spin current injector which avoids exchange-bias effect and make spin absorption method more reliable way to study spin Hall effect in antiferromagnetic material. We prepare a set of spin Hall device (SHD), reference lateral spin-valve and nano-Hall bar on the same substrate to test both Berry phase induced intrinsic anomalous Hall effect and spin Hall effect. We estimated λ_s , θ_{SH} and σ_{SH} of the nanocrystalline Mn_3Sn nanowire at room temperature and found σ_{SH} comparable to theoretical predictions[27, 42, 43]. Large anomalous Hall conductivity along with moderate spin Hall conductivity adds further functionality to Mn_3Sn for use in topological antiferromagnetic spintronics.

II. EXPERIMENTAL DETAILS

Lateral spin-valve devices and nano-Hall bars were fabricated on Si/SiO_2 (300 nm) substrate using e-beam lithography in three steps. In the first step of e-beam lithography a pair of 100 nm wide and 30 nm thick Py nanowires with distance of 1 μm were prepared by e-beam evaporation through a PMMA mask. The Py deposition was done in an UHV chamber with base pressure lower than 5×10^{-9} torr while substrate was kept at 10 $^\circ\text{C}$. In the second step Mn_3Sn nanowires were prepared using direct current (DC) magnetron sputtering. To avoid side walls in the nanowire MMA/PMMA bilayer was patterned by e-beam lithography to form a mask with undercut. Then Mn_3Sn was deposited at room temperature using DC sputtering at rate ~ 0.2 nm/s with 60 W of power and 0.3 Pa Ar gas pressure. We utilized 2 nm Ru seeding layer as a template to have smooth Mn_3Sn surface. After lift-off the nanowires were annealed in vacuum to 500 $^\circ\text{C}$ for 1 hours to achieve stoichiometric Mn_3Sn . We successfully fabricated 11.5 μm long, 50-70 nm thick and 150 nm wide nanowires which showed partly metallic electrical transport properties. Thinner nanowires showed semiconducting temperature dependence [See supplementary material for details [47]]. Recently we have used similar post annealing process to achieve high quality Mn_3Sn thin films [35]. The structural characterization of thin films prepared under similar sputtering conditions to the nanowire and nano-Hall bar were performed using x-ray diffractometer [47]. In the third step 100 nm wide and 100 nm thick Cu was thermally evaporated at rate $\sim 2\text{Å}/\text{s}$ in a separate UHV chamber with base pressure of $\sim 1.2 \times 10^{-9}$ torr. The surfaces of Py and Mn_3Sn nanowires were in-situ cleaned by Ar-ion milling for 40s before the Cu deposition. All the devices were capped with 2 nm AlO_x at the end to avoid oxidization. For comparative electrical and spin transport measurements one set of reference device, spin Hall device and nano-Hall bar were prepared together on the same substrate. Reference device and spin Hall devices are identical lateral spin valves except the Mn_3Sn nanowire was inserted in the middle of two Py electrodes in the later as shown in Fig. 2(a,b).

Multiple devices were fabricated on the same substrate to check reproducibility. All the electrical transport measurements were done using lock-in technique (173 Hz) in a He-4 flow cryostat.

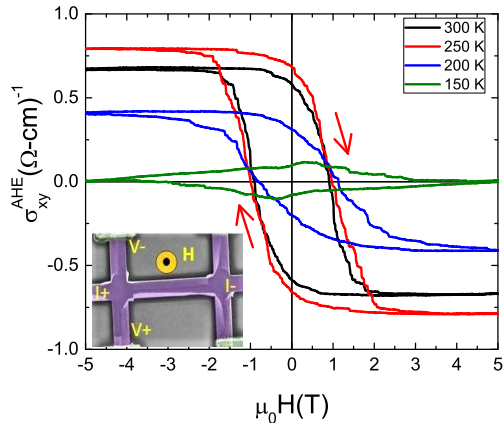


FIG. 1: Magnetic field dependence of the anomalous Hall conductivity ($\sigma_{xy}^{AHE} = -\frac{\rho_{xy}}{\rho_{xx}^2}$) measured at various temperatures between 150 to 300 K. Inset shows SEM picture of a Mn_3Sn nano-Hall bar (width = 500 nm, thickness = 70 nm, length = 3900 nm) with measurement configuration.

III. RESULTS AND DISCUSSION

Growth of Mn_3Sn thin films on thermally oxidized Si substrate strongly depends on the deposition temperature and the choice of seed layer like Ta, Ru or Pt [34, 48]. For our experiments we choose Ru underlayer due to its smaller spin Hall angle ($\theta_{SH} \approx 0.0056$) [49]. Nanocrystalline nanowires of Mn_3Sn with Ru seed layer were deposited on thermally oxidized silicon substrate at room temperature and post annealed ex-situ at 500 °C for crystallization. Bulk Mn_3Sn is known to possess different

magnetic structures depending on small alteration in the chemical composition and growth conditions [50]. The intrinsic AHE in Mn_3Sn depends sensitively on the magnetic structure and is maximized in the inverse triangular spin arrangement [29, 51]. In order to confirm intrinsic origin of anomalous Hall effect we measure anomalous Hall conductivity (σ_{xy}^{AHE}) in a nano-Hall bar prepared at the same time as the spin Hall devices. Fig. 1 shows magnetic field dependence of anomalous Hall conductivity, $\sigma_{xy}^{AHE} = -\frac{\rho_{xy}^{AHE}}{\rho_{xx}^2}$, at different temperatures after removal of the high-field linear background (ordinary Hall effect) from the measured data. Here anomalous Hall resistivity is defined as, $\rho_{xy}^{AHE} = \frac{V_{xy}}{I}t$, where V_{xy} is the Hall voltage, I is the applied current and t is the thickness of Mn_3Sn nano-Hall bar. The anomalous Hall conductivity show clear hysteresis loops with a considerable jump from $-0.6 (\Omega \text{ cm})^{-1}$ (for $\sigma_{xy}^{AHE}(H : +5T \rightarrow 0T)$) to $+0.6 (\Omega \text{ cm})^{-1}$ (for $\sigma_{xy}^{AHE}(H : -5T \rightarrow 0T)$) at room temperature. The anomalous Hall conductivity in Mn_3Sn changes its sign corresponding to the rotation of the Mn moments of the inverse triangular spin structure. The sign change in our nano-Hall bar occurs at field ~ 1 T which is comparable to that of Mn_3Sn polycrystalline thin film [35]. The higher switching field is related to polycrystalline nature of the Mn_3Sn films. The anomalous Hall conductivity was found to increase up to 250 K and disappear below 150 K as temperature was lowered. Bulk Mn_3Sn is known to undergo phase transition to an incommensurate spin spiral structure below 275 K which causes intrinsic contribution of anomalous Hall resistivity disappear below this temperature [51]. This transition temperature is quite sensitive to synthesis conditions which determine precise chemical composition (Mn:Sn ratio). The disappearance of AHE below 150 K in our nano-Hall bar is consistent with these observations in Mn_3Sn samples [51] indicating the inverse triangular spin structure at room temperature. In our experiments we primarily focus on room temperature measurements where inverse triangular structure-induced Berry curvature seems to be the dominant contributor to AHE.

Figure 2(a) and (b) presents schematic of a spin Hall and reference lateral spin-valve device, respectively. First, we affirm the quality of Mn_3Sn nanowire from temperature dependence of resistance measurement (see Supplementary material for further details). Ideal nanowire is expected to show metallic temperature dependence with resistivity $\rho \approx 320 \mu\Omega \text{ cm}$ at room temperature as in bulk Mn_3Sn [17]. Fig. 2(c) shows temperature dependence of the resistivity of a Mn_3Sn nanowire in the spin Hall device. The electrical resistivity exhibits a partly metallic

behavior with resistivity $\rho \approx 1133 \mu\Omega \text{ cm}$ at room temperature. Higher resistivity in the nanowire might be related to additional electron scattering from the surface as a consequence of reduced dimension [52]. Below 50 K an upturn in the resistivity was observed which is reminiscent of a spin-glass state. It is well known that in bulk Mn_3Sn a cluster glass phase appears below 50 K due to spin canting towards c-axis [17, 51]. Although in bulk single crystals no resistivity up-turn is observed below 50 K, in nanocrystalline nanowires blocked spins at the

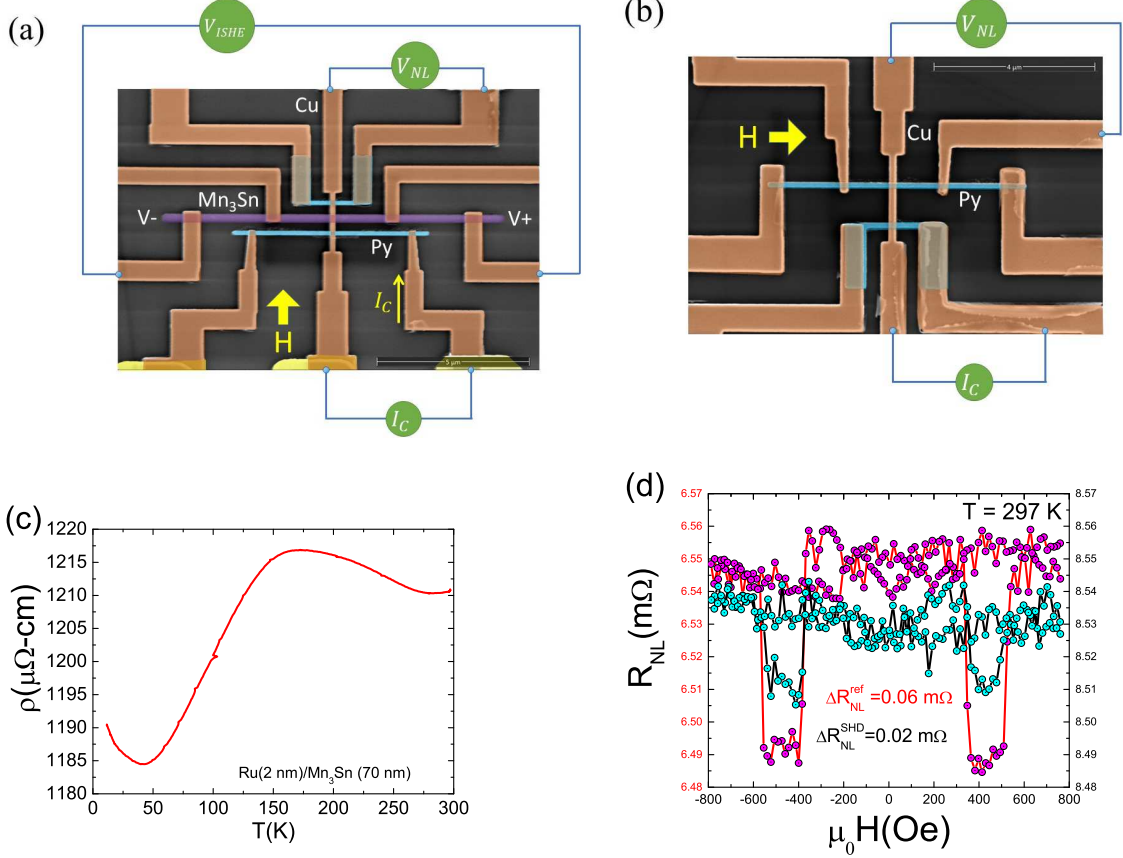


FIG. 2: Scanning electron microscopy (SEM) image of (a) spin Hall device (SHD) and (b) reference lateral spin valve device. The nonlocal and spin Hall measurement configuration are shown. In nonlocal measurement configuration magnetic field (H) is applied inplane along the long easy axis of Py while in spin Hall measurement configuration H is directed perpendicular (inplane) to it. (c) Resistivity of Mn₃Sn nanowire in the spin Hall device as a function of temperature. (d) Nonlocal resistance R_{NL} as a function of magnetic field for reference and spin Hall device measured at room temperature.

surface can cause Kondo-like up-turn in the resistivity.

Next, we performed spin absorption experiments in the nonlocal measurement configuration as shown in Fig. 2(a,b). In nonlocal spin signal measurements, a nonequilibrium spin accumulation is created inside Cu spin transport channel by injecting spin polarized current from one Py electrode into the Cu channel. The accumulated spin inside Cu diffuses towards the second Py detector electrode creating pure spin current. The nonlocal resistance is defined as, $R_{NL} = V_{NL}/I_C$, where V_{NL} is the nonlocal voltage at the detector and I_C is the charge current through the injector. When the Mn₃Sn nanowire is kept in contact with the Cu spin transport channel a part of the spin current is absorbed by it due to lower spin resistance of Mn₃Sn compared to Cu. The spin resistance is a quantity equivalent of electrical resistance but for spin current and is defined as, $R_S = \frac{\rho\lambda_s}{(1-p^2)A}$, where ρ is the resistivity, λ_s is the spin diffusion length, p is the spin polarization and A is the area of cross-section of the spin transport channel. In order to estimate amount of spin current absorbed by the Mn₃Sn

nanowire, nonlocal resistance was measured both in the spin Hall device (Fig. 2(a)) and another reference lateral spin valve device (Fig. 2(b)). The spin signal ΔR_{NL} is expressed as, $\Delta R_{NL} = R_{NL}^{\uparrow\uparrow} - R_{NL}^{\uparrow\downarrow}$, where $R_{NL}^{\uparrow\uparrow}$ ($R_{NL}^{\uparrow\downarrow}$) is the nonlocal resistance when both injector and detector Py are aligned parallel (antiparallel) to each other. Fig. 2(d) shows R_{NL} as a function of magnetic field for both spin Hall and reference lateral spin valve device at room temperature. Smaller ΔR_{NL} was observed in the spin Hall device compared to the reference lateral spin valve suggesting spin current absorption by Mn₃Sn nanowire. Similar spin current absorption was also observed at all temperature (see Supplementary material for measurement at 10 K)[47]. The spin resistance of Mn₃Sn nanowire can be obtained from ratio of spin signals between spin Hall (ΔR_{NL}^{SHD}) and reference lateral spin valve (ΔR_{NL}^{ref}) device. Assuming one dimensional spin diffusion and transparent interfaces the ratio of spin signals can be expressed as [53, 54]

$$\frac{\Delta R_{NL}^{SHD}}{\Delta R_{NL}^{ref}} = \frac{2Q_{Mn_3Sn} \left[\sinh\left(\frac{L}{\lambda_s(Cu)}\right) + 2Q_{Py} e^{L/\lambda_s(Cu)} + 2Q_{Py}^2 e^{L/\lambda_s(Cu)} \right]}{\left[\cosh\left(\frac{L}{\lambda_s(Cu)}\right) - \cosh\left(\frac{L-2d}{\lambda_s(Cu)}\right) + 2Q_{Py} \sinh\left(\frac{d}{\lambda_s(Cu)}\right) e^{(L-d)/\lambda_s(Cu)} + 2Q_{Mn_3Sn} \sinh\left(\frac{L}{\lambda_s(Cu)}\right) + 4Q_{Py} Q_{Mn_3Sn} e^{L/\lambda_s(Cu)} + 2Q_{Py} \sinh\left(\frac{L-d}{\lambda_s(Cu)}\right) e^{d/\lambda_s(Cu)} + 2Q_{Py}^2 e^{L/\lambda_s(Cu)} + 4Q_{Py}^2 Q_{Mn_3Sn} e^{L/\lambda_s(Cu)} \right]} \quad (1)$$

Where $Q_{Py(Mn_3Sn)} = \frac{R_{Py(Mn_3Sn)}}{R_{Cu}}$, with $R_{Cu} = \frac{\lambda_s(Cu)\rho_{Cu}}{w_{Cu}t_{Cu}}$, $R_{Py} = \frac{\lambda_s(Py)\rho_{Py}}{w_{Py}w_{Cu}(1-p_{Py}^2)}$ and $R_{Mn_3Sn} = \frac{\lambda_s(Mn_3Sn)\rho_{Mn_3Sn}}{w_{Mn_3Sn}w_{Cu}} \tanh\left(\frac{t_{Mn_3Sn}}{\lambda_s(Mn_3Sn)}\right)$ are the spin resistances of Cu, Py and Mn₃Sn nanowires, respectively. Here ρ_i , $\lambda_s(i)$, p_i , w_i and t_i are resistivity, spin diffusion length, spin polarization, width and thickness of corresponding nanowires, respectively ($i = \text{Py, Cu and Mn}_3\text{Sn}$). Here L is the center-to-center distance between two Py electrodes and d is the distance of the Mn₃Sn nanowire from injector Py electrode which was determined from SEM image of the device. The spin resistance values R_{Cu} and R_{Py} were taken from our previous work [55]. With measured value of the ratio $\frac{\Delta R_{NL}^{SHD}}{\Delta R_{NL}^{ref}}$, the spin resistance of Mn₃Sn nanowire can be obtained by solving Eq. 1. Using $\frac{\Delta R_{NL}^{SHD}}{\Delta R_{NL}^{ref}} = 0.33$, we found $R_{Mn_3Sn} = 0.2056 \Omega$. With resistivity of Mn₃Sn nanowire $\rho_{Mn_3Sn} \approx 1133 \mu\Omega \text{ cm}$ we estimate spin diffusion length of Mn₃Sn to be $\lambda_s(Mn_3Sn) \sim 0.75 \pm 0.67 \text{ nm}$ at room temperature. Recently, spin diffusion length has been measured in a variety of antiferromagnetic Mn alloys like IrMn, FeMn, PtMn and PdMn, etc., [56]. Spin diffusion length has been found to be quite short $\lambda_s \sim 1 \text{ nm}$ in all these antiferromagnets. Our calculated spin diffusion length for Mn₃Sn $\lambda_s(Mn_3Sn) \sim 0.75 \pm 0.67 \text{ nm}$ is consistent with these previous findings. Spin diffusion length also depends sensitively on the resistivity of the antiferromagnetic metal and can be further tuned with ρ_{Mn_3Sn} of the nanowire [1].

After estimating spin resistance of Mn₃Sn nanowire we switch the measurement configuration to the spin Hall measurement as shown in Fig. 2(a). In this measurement configuration magnetic field (H) is applied perpendicular and inplane to the long easy-axis of the Py nanowire as spin current \vec{I}_S , charge current \vec{I}_C and spin polarization \vec{s} are mutually orthogonal to each other as enforced by the equation, $\vec{I}_S = \frac{e}{\hbar} \theta_{SH} (\vec{I}_C \times \vec{s})$. Fig. 3(b) shows two-terminal resistance ($R-H$) of the Py nanowire as a function of magnetic field. This anisotropic magnetoresistance (AMR) or $R-H$ measurement reflects magnetization direction of the Py with respect to applied magnetic field H . The resistance is minimum when the

magnetization of Py nanowire is aligned along the applied field direction. Due to shape anisotropy the magnetization of Py nanowire is aligned along the long easy-axis in zero magnetic field. From Fig. 3(b) Py nanowire can be seen to saturate along the hard axis when $H > \pm 3000 \text{ Oe}$.

Alike previous measurement, pure spin current is created inside Cu channel by injecting charge current I_C through one of the Py electrode which is partially absorbed by the Mn₃Sn nanowire. Due to inverse spin Hall effect a charge current is produced inside the Mn₃Sn nanowire orthogonal to both the spin current \vec{I}_S and spin polarization \vec{s} direction. In open circuit condition a voltage drop V_{ISHE} is generated along the Mn₃Sn nanowire due to this charge current. The inverse spin Hall resistance is defined as, $R_{ISHE} = V_{ISHE}/I_C$, where I_C is the injected charge current through the Py electrode. When Py magnetization is switched with applied magnetic field the orientation of spin polarization changes causing opposite R_{ISHE} (or V_{ISHE}). The difference of the two R_{ISHE} yields twice the inverse spin Hall effect signal $2\Delta R_{ISHE}$. Fig. 3(a) shows R_{ISHE} as a function of magnetic field at room temperature. The measurement was done with injector current $I_C = 500 \mu\text{A}$. The inverse spin Hall resistance can be seen to saturate above $\pm 3000 \text{ Oe}$ when Py electrodes are aligned along the applied magnetic field. We found a small $2\Delta R_{ISHE} = 0.025 m\Omega$ from the difference between R_{ISHE} for the two spin polarization direction. The spin Hall resistivity can be calculated from the equation [53, 54, 57]

$$\rho_{SH} = -\frac{w_{Mn_3Sn}}{x_{sh}} \left(\frac{I_C}{I_S} \right) \Delta R_{ISHE}. \quad (2)$$

Where x_{sh} is the shunting factor which takes into account the charge current in the Mn₃Sn that is shunted through the more conductive Cu nanowire on top. The shunting factor x_{sh} can be calculated numerically using finite element method with COMSOL software (see Supplementary material for details). Here \vec{I}_S is the effective spin current that contributes to the ISHE voltage in Mn₃Sn and can be expressed as [53, 54]

$$\frac{\bar{I}_s}{I_c} = \frac{\lambda_s(Mn_3Sn)}{t_{Mn_3Sn}} \frac{(1 - e^{-t_{Mn_3Sn}/\lambda_s(Mn_3Sn)})^2}{(1 - e^{-2t_{Mn_3Sn}/\lambda_s(Mn_3Sn)})} \times \left[2\alpha_{Py} [Q_{Py} \sinh\left(\frac{L-d}{\lambda_s(Cu)}\right) + Q_{Py}^2 e^{\frac{L-d}{\lambda_s(Cu)}}] \right]$$

$$\left[\cosh\left(\frac{L}{\lambda_s(Cu)}\right) - \cosh\left(\frac{L-2d}{\lambda_s(Cu)}\right) + 2Q_{Py} \sinh\left(\frac{d}{\lambda_s(Cu)}\right) e^{\frac{L-d}{\lambda_s(Cu)}} + 2Q_{Mn_3Sn} \sinh\left(\frac{L}{\lambda_s(Cu)}\right) + 4Q_{Py}Q_{Mn_3Sn} e^{\frac{L}{\lambda_s(Cu)}} + 2Q_{Py} e^{\frac{d}{\lambda_s(Cu)}} \sinh\left(\frac{L-d}{\lambda_s(Cu)}\right) + 2Q_{Py}^2 e^{\frac{L}{\lambda_s(Cu)}} + 4Q_{Py}^2 Q_{Mn_3Sn} e^{\frac{L}{\lambda_s(Cu)}} \right]$$
(3)

Using Eqs. 2 and 3, we found $\rho_{SH} = -60.33 \pm 26.48 \mu\Omega \text{ cm}$. The spin Hall angle given by the ratio of spin Hall resistivity against electrical resistivity can be calculated as, $\theta_{SH} = -\frac{\rho_{SH}}{\rho_{Mn_3Sn}}$, where $\rho_{Mn_3Sn} = 1133 \mu\Omega \text{ cm}$ is resistivity of the Mn_3Sn nanowire[59]. We estimate $\theta_{SH} = 0.053 \pm 0.024$ for our Mn_3Sn nanowire which is comparable to θ_{SH} of 4d and 5d transition heavy metals determined by similar spin absorption method [57, 58]. The spin Hall resistivity is related to spin hall conductivity as, $\sigma_{SH} \approx -\frac{\rho_{SH}}{\rho_{Mn_3Sn}^2}$. We found $\sigma_{SH} = 46.99 \pm 3.42 \left(\frac{\hbar}{e}\right) (\Omega \text{ cm})^{-1}$. Recent theoretical investigations have predicted a positive sign of intrinsic spin Hall conductivity for Mn_3Sn and magnitude in the range $\sigma_{SH}^{int} \sim 36-96 \left(\frac{\hbar}{e}\right) (\Omega \text{ cm})^{-1}$ [27, 42, 43]. Our estimated σ_{SH} is within the range of these theoretical predictions based on Berry curvature calculations. Recently, Mn-Sn alloy films has shown to exhibit a large spin Hall angle [60]. However, spin Hall angle was found to be negative in that case. Positive spin Hall angle observed in our case suggest measured inverse spin Hall signal does not originate from impurity phases. In Eq. 2, we assume that all the absorbed spin current is converted to electrical voltage via inverse spin Hall effect. However, there might be other sources of spin memory loss related to magnetization dynamics inside the antiferromagnet. It is quite challenging to estimate this exactly and is the main bottleneck of spin absorption method for antiferromagnetic material.

Nanowire used in this work are nanocrystalline and contain randomly oriented Kagome planes[47]. As per theoretical predictions in order to observe large σ_{SH} , one should set the charge and spin currents inside the Kagome plane [42]. Our results are comparable to structurally similar material $IrMn_3$ which also shows spin diffusion length less than 1 nm and spin Hall angle vary between $\theta_{SH} = 3-12\%$ depending of composition x of $Ir_{1-x}Mn_x$ [44]. In $IrMn_3$ spin Hall effect is believed to originate from two sources, (i) bulk spin-orbit coupling of $IrMn_3$ and (ii) the triangular spin structure also gives rise to an intrinsic spin Hall effect that is large and strongly depends on the crystallographic orientation of the epitaxial film. Highly oriented Mn_3Sn nanowires may be needed in order to observe theoretically predicted odd spin cur-

rents related to inverse triangular spin structure[45]. Recently, we have observed that the spin Hall angle in single crystal Mn_3Sn can be switched with the direction of the staggered moment in the inverse triangular spin structure [61].

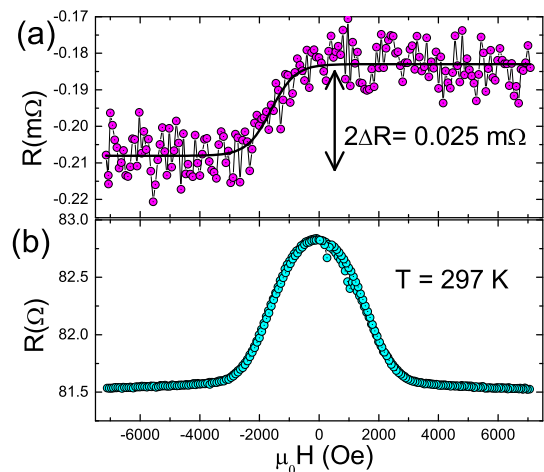


FIG. 3: (a) Magnetic field dependence of Inverse spin Hall resistance R_{ISHE} measured at room temperature. The inverse spin Hall resistance R_{ISHE} saturates above ± 3000 Oe when Py magnetization is aligned along applied magnetic field. The difference between positive and negative saturated R_{ISHE} is called inverse spin Hall signal $2\Delta R_{ISHE}$. (b) Anisotropic magnetoresistance (AMR) of the Py nanowire in the same device. The spin polarization direction \vec{s} of the spin current \vec{I}_s is determined by the magnetization direction of Py injector electrode.

IV. CONCLUSIONS

To summarize we have investigated inverse spin Hall effect in nanocrystalline Mn_3Sn nanowires by spin absorption method. We have estimated positive spin Hall angle $\theta_{SH} \sim 5.3 \pm 2.4\%$, spin diffusion length $\lambda_s(Mn_3Sn) \sim 0.75 \pm 0.67$ nm and spin Hall conductivity $\sigma_{SH} \sim 46.9$

± 3.4 (\hbar/e) ($\Omega \text{ cm}$)⁻¹. This σ_{SH} is quite close to theoretically predicted intrinsic spin Hall conductivity of Mn₃Sn suggesting intrinsic origin of spin Hall effect in our nanowires[27, 42, 43]. The spin Hall and anomalous Hall conductivity can be further improved by resistivity, strain[62] and chemical tuning[31] of the present Mn₃Sn nanowire. These results are obtained in a nanocrystalline nanowire which may have random orientations of Kagome planes. Further structural characterization is required on the nanowires to understand detailed spin structure and orientation of Kagome planes. With highly oriented nanowires it might be possible to investigate theoretically predicted novel odd spin currents resulting from the noncollinear magnetic structure. Reasonably large spin Hall conductivity of Mn₃Sn comparable to other Mn-alloy based antiferromagnets [56] suggest it can

be used as an efficient spin current detector in nanometer-sized antiferromagnetic devices. Inclusion of spin Hall effect further broadens great potential of Mn₃Sn in the antiferromagnetic spintronic devices that could enable spin-based operations at the ultimate THz frequencies.

Acknowledgments

We thank Dr Y. Niimi, Dr E. Sagasta, Prof Fèlix Casanova and Prof S. P. Dash for helpful discussions. This work was supported by CREST(JPMJCR15Q5), Grant-in-Aid for Scientific Research on Innovative Area (Grant No. 26103002, 15H05882 and 15H05883) from the Ministry of Education, Culture, Sports, Science, and Technology of Japan. Lithography facilities provided by Dr. T. Nakamura and Prof. S. Katsumoto is gratefully acknowledged.

-
- [1] V. Baltz, A. Manchon, M. Tsoi, T. Moriyama, T. Ono, and Y. Tserkovnyak, *Rev. Mod. Phys.* **90**, 015005 (2018).
- [2] L. Šmejkal, T. Jungwirth, and J. Sinova, *Phys. Status Solidi RRL* **11**, 1700044 (2017).
- [3] L. Šmejkal, Y. Mokrousov, B. Yan, and A. H. MacDonald, *Nat. Phys.* **14**, 242 (2018).
- [4] V. M. T. S. Barthem, C. V. Colin, H. Mayaffre, M.-H. Julien, and D. Givord, *Nat. Commun.* **4**, 2892 (2013).
- [5] P. Wadley, B. Howells, J. Zelezny, C. Andrews, V. Hills, R. P. Campion, V. Novak, K. Olejnik, F. Maccherozzi, S. S. Dhesi, S. Y. Martin, T. Wagner, J. Wunderlich, F. Freimuth, Y. Mokrousov, J. Kunes, J. S. Chauhan, M. J. Grzybowski, A. W. Rushforth, K. W. Edmonds, B. L. Gallagher, and T. Jungwirth, *Science* **351**, 587 (2016).
- [6] J. Železný, P. Wadley, K. Olejnik, A. Hoffmann, and H. Ohno, *Nat. Phys.* **14**, 220 (2018).
- [7] J. Park, G. Lee, F. Wolff-Fabris, Y. Y. Koh, M. J. Eom, Y. K. Kim, M. A. Farhan, Y. J. Jo, C. Kim, J. H. Shim, and J. S. Kim, *Phys. Rev. Lett.* **107**, 126402 (2011).
- [8] H. Masuda, H. Sakai, M. Tokunaga, Y. Yamasaki, A. Miyake, J. Shiozaki, S. Nakamura, S. Awaji, A. Tsukazaki, H. Nakao, Y. Murakami, T.-h. Arima, Y. Tokura, and S. Ishiwata, *Sci. Adv.* **2**, e1501117 (2016).
- [9] P. Richard, K. Nakayama, T. Sato, M. Neupane, Y.-M. Xu, J. H. Bowen, G. F. Chen, J. L. Luo, N. L. Wang, X. Dai, Z. Fang, H. Ding, and T. Takahashi, *Phys. Rev. Lett.* **104**, 137001 (2010).
- [10] A. Wang, I. Zaliznyak, W. Ren, L. Wu, D. Graf, V. O. Garlea, J. B. Warren, E. Bozin, Y. Zhu, and C. Petrovic, *Phys. Rev. B* **94**, 165161 (2016).
- [11] R. A. Müller, N. R. Lee-Hone, L. Lapointe, D. H. Ryan, T. Pereg-Barnea, A. D. Bianchi, Y. Mozharivskyj, and R. Flacau, *Phys. Rev. B* **90**, 041109(R) (2014).
- [12] M. Hirschberger, S. Kushwaha, Z. Wang, Q. Gibson, S. Liang, C. A. Belvin, B. A. Bernevig, R. J. Cava, and N. P. Ong, *Nat. Mater.* **15**, 1161 (2016).
- [13] Z. F. Wang, H. Zhang, D. Liu, C. Liu, C. Tang, C. Song, Y. Zhong, J. Peng, F. Li, C. Nie, L. Wang, X. J. Zhou, X. Ma, Q. K. Xue, and F. Liu, *Nat. Mater.* **15**, 968 (2016).
- [14] N. Wakeham, E. D. Bauer, M. Neupane, and F. Ronning, *Phys. Rev. B* **93**, 205152 (2016).
- [15] A. B. Sushkov, J. B. Hofmann, G. S. Jenkins, J. Ishikawa, S. Nakatsuji, S. Das Sarma, and H. D. Drew, *Phys. Rev. B* **92**, 241108(R) (2015).
- [16] H. Chen, Q. Niu, and A. H. MacDonald, *Phys. Rev. Lett.* **112**, 017205 (2014).
- [17] S. Nakatsuji, N. Kiyohara, and T. Higo, *Nature (London)* **527**, 212 (2015).
- [18] A. K. Nayak, J. E. Fischer, Y. Sun, B. Yan, J. Karel, A. C. Komarek, C. Shekhar, N. Kumar, W. Schnelle, J. Kübler, C. Felser, and S. S. P. Parkin, *Sci. Adv.* **2**, e1501870 (2016).
- [19] K. Manna, Y. Sun, L. Mchler, J. Kübler, and C. Felser, *Nat. Rev. Mater.* **3**, 244 (2018).
- [20] N. Kiyohara, T. Tomita, and S. Nakatsuji, *Phys. Rev. Appl.* **5**, 064009 (2016).
- [21] J. Kübler, C. Felser, *Europhys. Lett.* **108**, 67001 (2014).
- [22] J. Kübler and C. Felser, *Europhys. Lett.* **120**, 47002 (2017).
- [23] H. Yang, Y. Sun, Y. Zhang, W.-J. Shi, S. S. P. Parkin, and B. Yan, *New J. Phys.* **19**, 015008 (2017).
- [24] S. Nakatsuji, T. Higo, M. Ikhlas, T. Tomita, and Z. Tian, *Philos. Mag.* **97**, 2815 (2017).
- [25] P. J. Brown, V. Nunez, F. Tasset, J. B. Forsyth, and P. Radhakrishna, *J. Phys.: Condens. Matter* **2**, 9409 (1990).
- [26] T. Nagamiya, S. Tomiyoshi, Y. Yamaguchi, *Solid State Commun.* **42**, 385.388 (1982).
- [27] G. Guo and T. Wang, *Phys. Rev. B* **96**, 224415 (2017).
- [28] K. Kuroda, T. Tomita, M.-T. Suzuki, C. Bareille, A. A. Nugroho, P. Goswami, M. Ochi, M. Ikhlas, M. Nakayama, S. Akebi, R. Noguchi, R. Ishii, N. Inami, K. Ono, H. Kumigashira, A. Varykhalov, T. Muro, T. Koretsune, R. Arita, S. Shin, T. Kondo, and S. Nakatsuji, *Nat. Mater.* **16**, 1090 (2017).
- [29] X. Li, L. Xu, L. Ding, J. Wang, M. Shen, X. Lu, Z. Zhu, and K. Behnia, *Phys. Rev. Lett.* **119**, 056601 (2017).
- [30] H. Narita, M. Ikhlas, M. Kimata, A. A. Nugroho, S. Nakatsuji, and Y. Otani, *Appl. Phys. Lett.* **111**, 202404 (2017).
- [31] M. Ikhlas, T. Tomita, T. Koretsune, M.-T. Suzuki, D. Nishio-Hamane, R. Arita, Y. Otani, and S. Nakatsuji, *Nat. Phys.* **13**, 1085 (2017).
- [32] X. Li, L. Xu, H. Zuo, A. Subedi, Z. Zhu, K. Behnia, *SciPost Phys.* **5**, 063 (2018).

- [33] T. Higo, H. Man, D. B. Gopman, L. Wu, T. Koretsune, O. M. J. van't Erve, Y. P. Kabanov, D. Rees, Y. Li, M.-T. Suzuki, S. Patankar, M. Ikhlas, C. L. Chien, R. Arita, R. D. Shull, J. Orenstein, and S. Nakatsuji, *Nat. Photonics* **12**, 73 (2018).
- [34] A. Markou, J. M. Taylor, A. Kalache, P. Werner, S. S. P. Parkin, and C. Felser, *Phys. Rev. Mater.* **2**, 051001(R) (2018).
- [35] T. Higo, D. Qu, Y. Li, C. L. Chien, Y. Otani and S. Nakatsuji, *Appl. Phys. Lett.* **113**, 202402 (2018).
- [36] Y. You, X. Chen, X. Zhou, Y. Gu, R. Zhang, F. Pan, C. Song, *Adv. Electron. Mater.* 1800818 (2019).
- [37] G. Y. Guo, S. Murakami, T.-W. Chen, and N. Nagaosa, *Phys. Rev. Lett.* **100**, 096401 (2008).
- [38] N. Nagaosa, J. Sinova, S. Onoda, A. H. MacDonald, and N. P. Ong, *Rev. Mod. Phys.* **82**, 1539 (2010).
- [39] T. Jungwirth, Q. Niu, and A. H. MacDonald, *Phys. Rev. Lett.* **88**, 207208, (2002).
- [40] Y. Omori, E. Sagasta, Y. Niimi, M. Gradhand, L.-E. Hueso, F. Casanova and Y. Otani, *Phys. Rev. B* **99**, 014403 (2019).
- [41] Y. Sun, Y. Zhang, C. Felser, and B. Yan, *Phys. Rev. Lett.* **117**, 146403 (2016).
- [42] Y. Zhang, Y. Sun, H. Yang, J. Železný, S. P. P. Parkin, C. Felser, and B. Yan, *Phys. Rev. B* **95**, 075128 (2017).
- [43] Y. Zhang, J. Železný, Y. Sun, J. van den Brink, and B. Yan, *New J. Phys.* **20**, 073028 (2018).
- [44] W. Zhang, W. Han, S.-H. Yang, Y. Sun, Y. Zhang, B. Yan, and S. S. P. Parkin, *Sci. Adv.* **2**, e1600759 (2016).
- [45] J. Železný, Y. Zhang, C. Felser, and B. Yan, *Phys. Rev. Lett.* **119**, 187204 (2017).
- [46] H. Chen, Q. Niu, and A. H. MacDonald, *arXiv:1803.01294v1*
- [47] See Supplemental Material at <http://link.aps.org/supplemental/> for details of the nanowire fabrication process, x-ray diffraction of Mn₃Sn thin film, RT of nano-Hall bar, calculation of shunting factor x_{sh} by COMSOL software, spin absorption measurement at 10 K and reproducibility data.
- [48] P. C. Filippou, J. Jeong, Y. Ferrante, S.-H. Yang, T. Topuria, M. G. Samant and S. S. P. Parkin, *Nat. Commun.* **9**, 4653 (2018).
- [49] Z. C. Wen, J. Kim, H. Sukegawa, M. Hayashi, and S. Mitani, *AIP Adv.* **6**, 056307 (2016).
- [50] G. J. Zimmer and E. Krén, *AIP Conf. Proc.* **5**, 513 (1972); E. Kren, J. Paitz, G. Zimmer, and É. Zsoldos, *Physica B* **80**, 226 (1975).
- [51] N. H. Sung, F. Ronning, J. D. Thompson, and E. D. Bauer, *Appl. Phys. Lett.* **112**, 132406 (2018).
- [52] K. Fuchs, *Proc. Cambridge Philos. Soc.* **34**, 100 (1938); E. H. Sondheimer, *Adv. Phys.* **1**, 1 (1952); A. F. Mayadas and M. Shatzkes, *Phys. Rev. B* **1**, 1382 (1970).
- [53] E. Sagasta, Y. Omori, M. Isasa, M. Gradhand, L. E. Hueso, Y. Niimi, Y. Otani, and F. Casanova, *Phys. Rev. B* **94**, 060412(R) (2016).
- [54] E. Sagasta, Y. Omori, S. Véz, R. Llopis, C. Tollan, A. Chuvilin, L. E. Hueso, M. Gradhand, Y. Otani, and F. Casanova, *Phys. Rev. B* **98**, 060410(R) (2018).
- [55] P. K. Muduli, M. Kimata, Y. Omori, T. Wakamura, S. P. Dash, Y. C. Otani, *Phys. Rev. B* **98**, 024416 (2018).
- [56] W. Zhang, M. B. Jungfleisch, W. Jiang, J. E. Pearson, A. Hoffmann, F. Freimuth, and Y. Mokrousov, *Phys. Rev. Lett.* **113**, 196602 (2014).
- [57] M. Morota, Y. Niimi, K. Ohnishi, D. H. Wei, T. Tanaka, H. Kontani, T. Kimura and Y. Otani, *Phys. Rev. B* **83**, 174405 (2011).
- [58] Y. Niimi, and Y. Otani, *Rep. Prog. Phys.* **78**, 124501 (2015).
- [59] The resistivity value of Mn₃Sn nanowire used in the calculation is $\rho_{Mn_3Sn} \approx 1133 \mu\Omega \text{ cm}$. If the calculation is replicated for bulk resistivity $\rho_{Mn_3Sn} \approx 320 \mu\Omega \text{ cm}$, we obtain $\theta_{SH} \sim 5.34 \%$, spin diffusion length $\lambda_s(Mn_3Sn) \sim 2.64 \text{ nm}$ and spin Hall conductivity $\sigma_{SH} \sim 167.06 (\hbar/e) (\Omega \text{ cm})^{-1}$. Note that spin Hall angle remains unchanged due to increase in $\lambda_s(Mn_3Sn)$ for lower ρ_{Mn_3Sn} .
- [60] D. Qu, T. Higo, T. Nishikawa, K. Matsumoto, K. Kondou, D. Nishio-Hamane, R. Ishii, P. K. Muduli, Y. Otani, and S. Nakatsuji, *Phys. Rev. Materials* **2**, 102001(R) (2018).
- [61] M. Kimata, H. Chen, K. Kondou, S. Sugimoto, P. K. Muduli, M. Ikhlas, Y. Omori, T. Tomita, A. H. MacDonald, Satoru Nakatsuji, YoshiChika Otani, *Nature* **565**, 627 (2019).
- [62] Z. Q. Liu, H. Chen, J. M. Wang, J. H. Liu, K. Wang, Z. X. Feng, H. Yan, X. R. Wang, C. B. Jiang, J. M. D. Coey and A. H. MacDonald, *Nat. Electron.* **1**, 172 (2018).

Supplementary Material

Evaluation of spin diffusion length and spin Hall angle of antiferromagnetic Weyl semimetal Mn_3Sn .

P. K. Muduli¹, T. Higo¹, T. Nishikawa¹, Danru Qu¹, H. Isshiki¹, K. Kondou², D. Nishio-Hamane¹, S. Nakatsuji¹, YoshiChika Otani^{1,2}

¹*Institute for Solid State Physics, University of Tokyo, Kashiwa 277-8581, Japan*

²*Center for Emergent Matter Science, RIKEN, 2-1 Hirosawa, Wako 351-0198, Japan*

I. QUALITY OF Mn_3Sn NANOWIRE

Fabrication of high-quality nanowires with thickness ~ 10 -50 nm and width ~ 100 -200 nm are experimentally quite challenging. In this manuscript we follow a bottom up approach for device fabrication. The Mn_3Sn nanowires were deposited by DC sputtering method on MMA/PMMA mask prepared by e-beam lithography. Ideally thinner nanowires with thickness comparable to its' spin diffusion length are most suitable for spin-absorption experiments. In our experiments we used thicker ~ 70 nm nanowires as thinner (< 50 nm) nanowires were found to show semiconducting-like $R(T)$ probably due to oxidation in atmosphere.

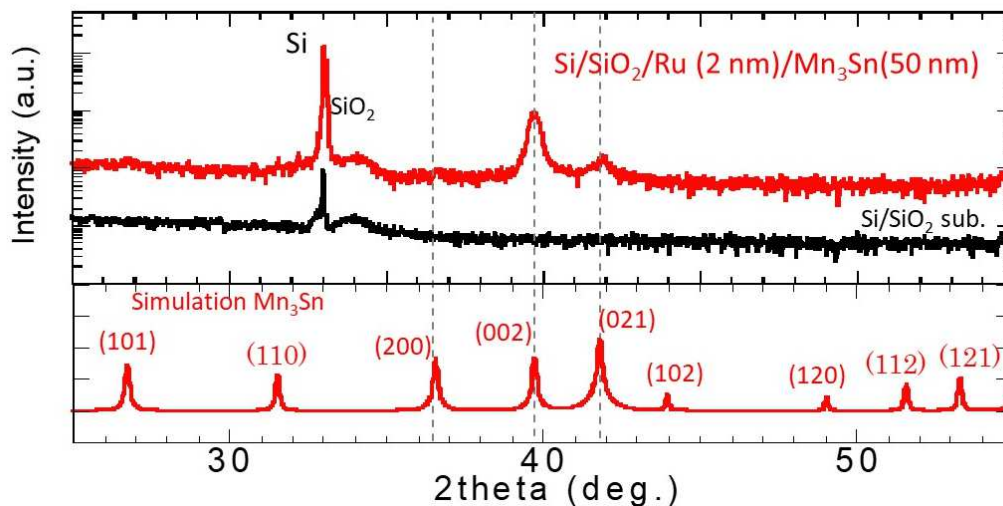


FIG. S1: X-ray diffraction scan of 50 nm Mn_3Sn thin film with 2 nm Ru seed layer (red) and bare Si/SiO_2 substrate (black). Bottom panel shows simulated x-ray diffraction pattern of Mn_3Sn with all possible peaks indexed.

Besides nanowires, Mn_3Sn thin films were also fabricated under identical sputtering condition for structural characterization. Note that thin films were annealed insitu while nanowires were annealed ex-situ after the lift-off process. Therefore, nanowires might be more disordered compared to thin films. Fig. S1 shows x-ray diffraction spectra of a 50 nm thick Mn_3Sn film with 2 nm Ru seed layer. For comparison x-ray diffraction spectra of one bare Si/SiO_2 substrate without Mn_3Sn film is also plotted. Bottom panel shows simulated x-ray diffraction spectra of the hexagonal Mn_3Sn structure with all crystallographic directions indexed. Broad peaks corresponding to (002), (021) and (200) plane of Mn_3Sn were detected confirming polycrystalline nature of the films. A more intense (002) peak was observed suggesting preferential hexagonal (0001)-axis oriented texture of the films.

Many of the nanowires were found to be unstable and change from metallic to semiconducting $R(T)$ during or soon after measurement. This suggest these nanowires are probably inhomogeneous and may contain metallic and insulating patches. In the manuscript we report one typical measurement on the nanowires which show partly metallic behavior as in Fig. S2(d). The nano-Hall bar prepared at the same time showed stable metallic $R(T)$ (as in Fig. S3) and anomalous Hall effect at room temperature. We would like to emphasize that irrespective of metallic or

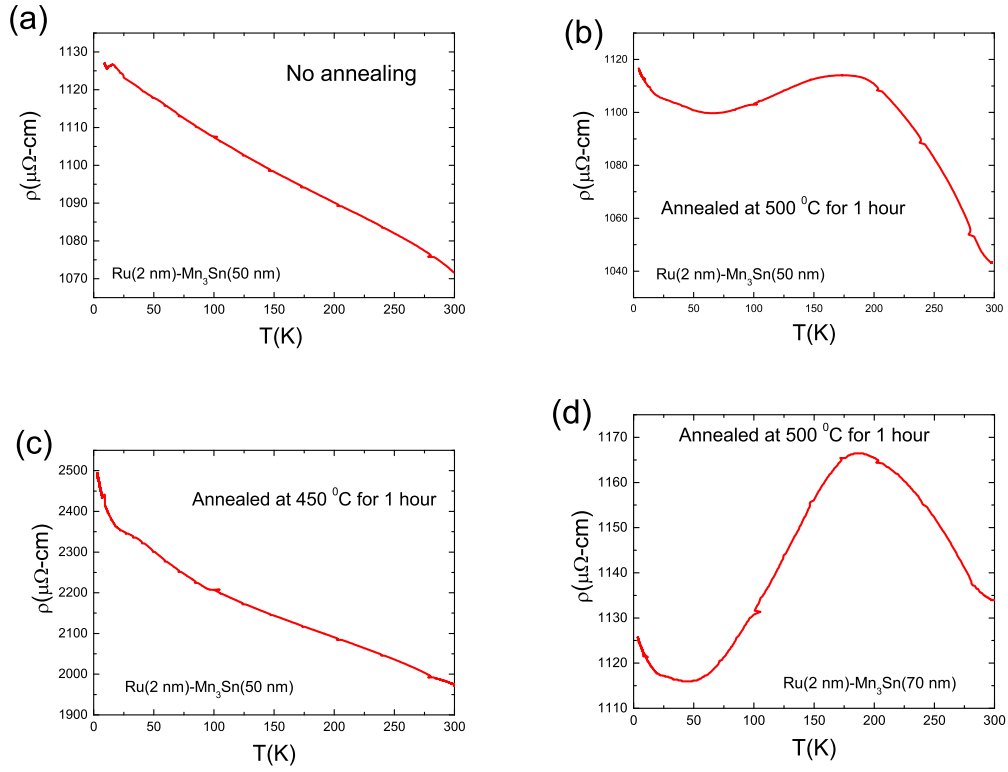


FIG. S2: (a) Temperature dependence of resistance of Mn_3Sn nanowire without post annealing. Nano-Hall bar prepared together with this nanowire did not showed AHE at room temperature. (b,c,d) Temperature dependence of resistance of different type of nanowires obtained after annealing at $450\text{ }^\circ\text{C}$ and $500\text{ }^\circ\text{C}$ for 1 hour. Nano-Hall bars prepared together with this nanowire showed AHE at room temperature.

semiconducting $R(T)$ all the nanowires showed inverse spin Hall effect (ISHE) signal at room temperature. We believe the ISHE signal at room temperature primarily originates from Mn_3Sn phase as Mn-Sn alloy phases have opposite sign of spin Hall angle.

II. TEMPERATURE DEPENDENT RESISTIVITY OF Mn_3Sn NANO-HALL BAR

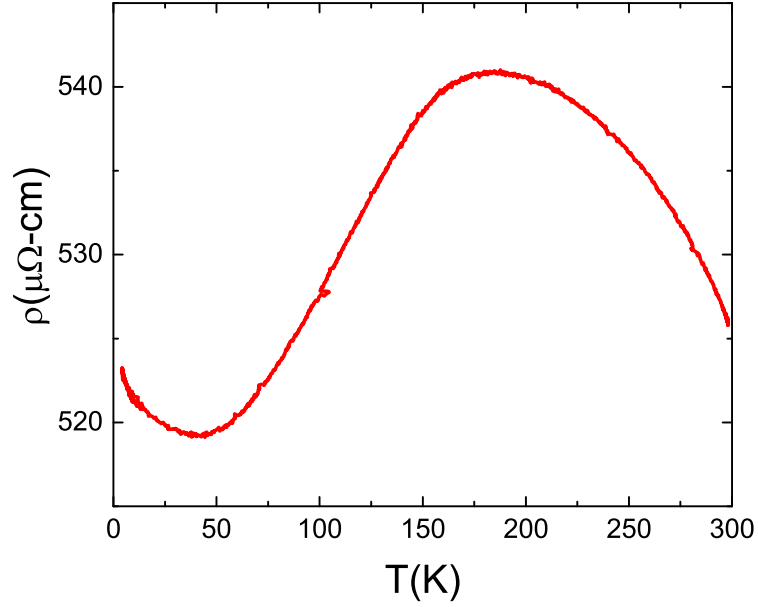


FIG. S3: Shows temperature dependence of resistance of a nano-Hall bar structure. The resistivity is defined as $\rho = \frac{V}{I} \times \frac{wt}{L}$, where $V(I)$ is the longitudinal voltage(current), $w(= 500 \text{ nm})$ is the width, $L (= 3900 \text{ nm})$ is the length and $t(= 70 \text{ nm})$ is the thickness of nano-Hall bar. Note that nano-Hall bar has lower resistivity than nanowires ($w = 200 \text{ nm}$) due to larger width ($w = 500 \text{ nm}$) of the Hall bar.

III. SHUNTING FACTOR CALCULATION

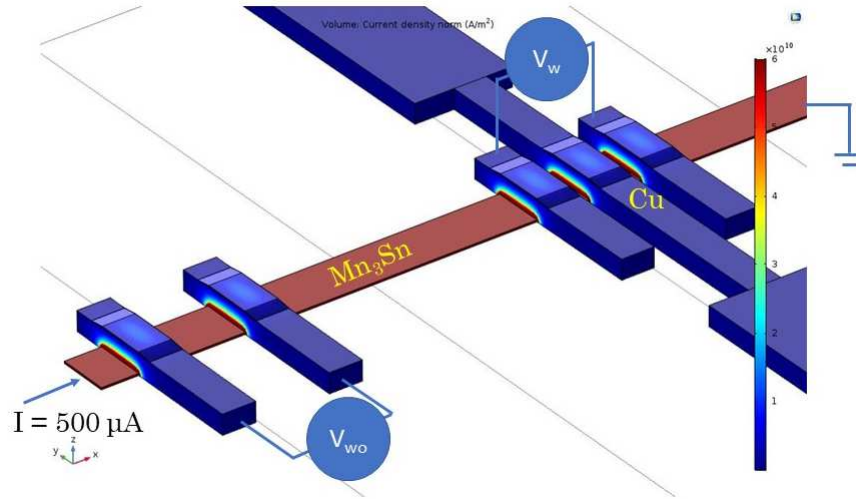


FIG. S4: COMSOL simulation result of current density in the shunt-device. To determine x , $I = 500 \mu\text{A}$ was passed through the Mn₃Sn nanowire and voltages V_w and V_{wo} was measured from the simulation.

The spin Hall angle and spin Hall conductivity critically depends on the shunting factor x , which determines amount of charge current that is shunted back to Cu after spin-charge conversion in the spin Hall material. In order to estimate x we use a shunt device (as shown in Fig. S4) that was used previously in [1]. We use COMSOL AC/DC module to calculate current distribution in this shunt device. As x critically depends on the width of nanowires in the device, we measure exact dimension of the spin Hall device under consideration with SEM and found $w_{Cu} = 165 \text{ nm}$ and $w_{Mn_3Sn} = 256 \text{ nm}$. The COMSOL simulation was done in a shunting device with center-to-center distance $L = 530 \text{ nm}$, $\rho_{Cu} = 3.72 \mu\Omega \text{ cm}$, and $\rho_{Mn_3Sn} = 1133 \mu\Omega \text{ cm}$. The shunting factor x can be calculated using the equation [1,2],

$$\frac{V_w}{V_{wo}} = \frac{L + 2w_{Cu}(x - 1)}{L + w_{Cu}(x - 1)} = \frac{40 + 66x}{73 + 33x} \quad (\text{S1})$$

In this simulation we ignore side shunting by reducing thickness of spin Hall material to 10 nm. Note that Eq. S1 is valid only for shunting from top side and is inaccurate in presence of significant side shunting when thickness of spin Hall material is comparable to Cu thickness. From COMSOL simulation we found $V_w = 0.4748 \text{ V}$ and $V_{wo} = -0.8236 \text{ V}$. Using Eq. S1 we found $x = 0.04$ for our device. Fig. S5 shows variation of spin Hall angle and spin Hall conductivity with shunting factor x in the range 0.01 to 0.1.

[1] Y. Niimi, M. Morota, D. H. Wei, C. Deranlot, M. Basletic, A. Hamzic, A. Fert, and Y. Otani, Phys. Rev. Lett. 106, 126601 (2011).

[2] PhD Thesis, Miren Isasa Gabilondo, CIC nanoGUNE.

[3] M. Isasa, M. C. Martínez-Velarte, E. Villamor, C. Magón, L. Morellón, J. M. De Teresa, M. R. Ibarra, G. Vignale, E. V. Chulkov, E. E. Krasovskii, L. E. Hueso, and F. Casanova, Phys. Rev. B 93, 014420 (2016).

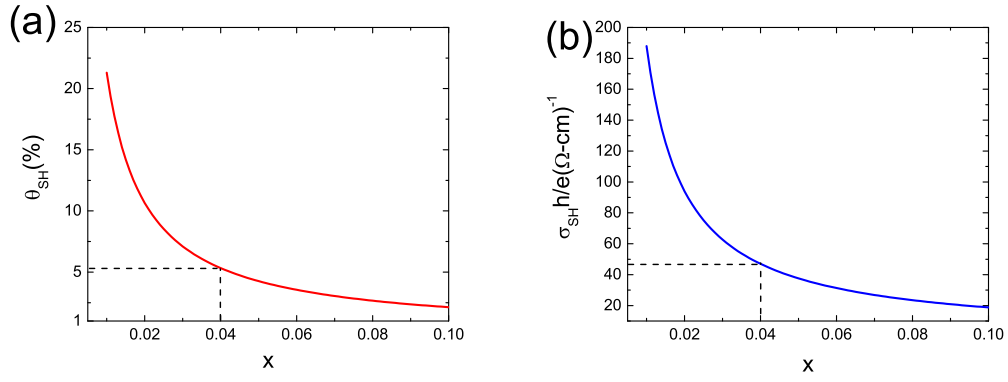


FIG. S5: Variation of (a) spin Hall angle θ_{SH} and (b) spin Hall conductivity σ_{SH} with shunting factor x in the range 0.01 to 0.1. Note that $x = 0.1$ is the maximum value of shunting factor reported [3] experimentally in these devices with resistivity of spin Hall material of the order of $\sim 900 \mu\Omega\text{-cm}$.

IV. SPIN ABSORPTION MEASUREMENT AT 10 K.

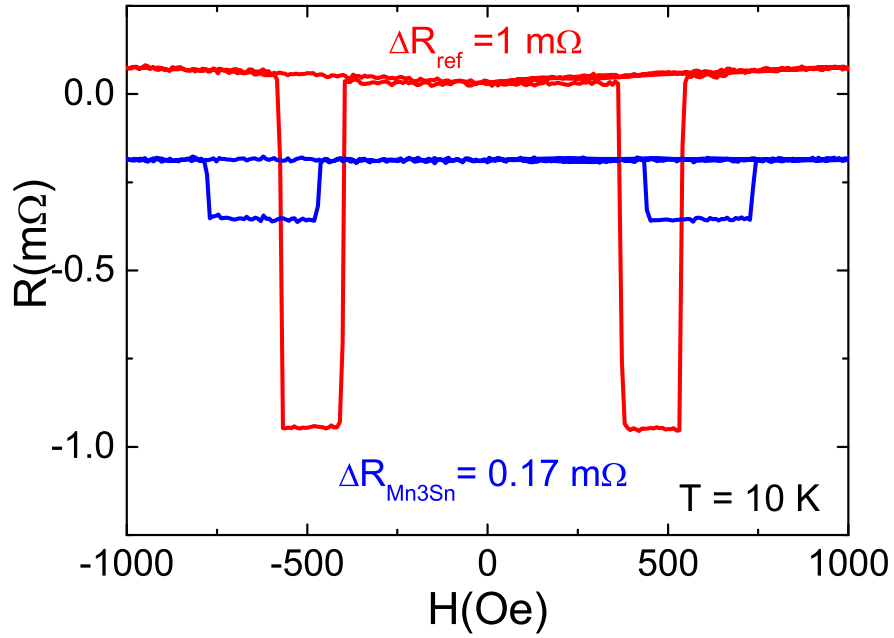


FIG. S6: Shows Nonlocal resistance R_{NL} as a function of magnetic field for reference (red) and spin Hall device (blue) measured at 10 K. Measurement done at room temperature on the same devices is presented in the main text

V. REPRODUCIBILITY

Most of the freshly prepared nanowires showed inverse spin Hall effect (ISHE) signal at room temperature. Although magnitude of ISHE signal was found to vary from device to device.

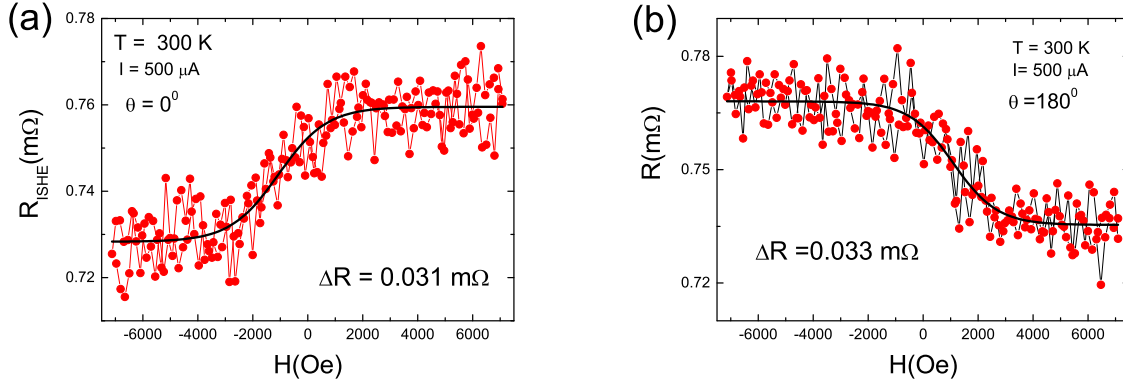


FIG. S7: Magnetic field dependence of inverse spin Hall resistance R_{ISHE} measured at room temperature for magnetic field applied at (a) $\theta = 0^\circ$ and (b) $\theta = 180^\circ$. Magnetic field angle $\theta = 0^\circ$ corresponds to field applied in-plane along Cu spin transport channel which is perpendicular to Mn_3Sn nanowire (direction as shown in Fig. 2(a)). This ISHE signal measurement is obtained in the semiconducting Mn_3Sn nanowire shown in Fig. S2(c).

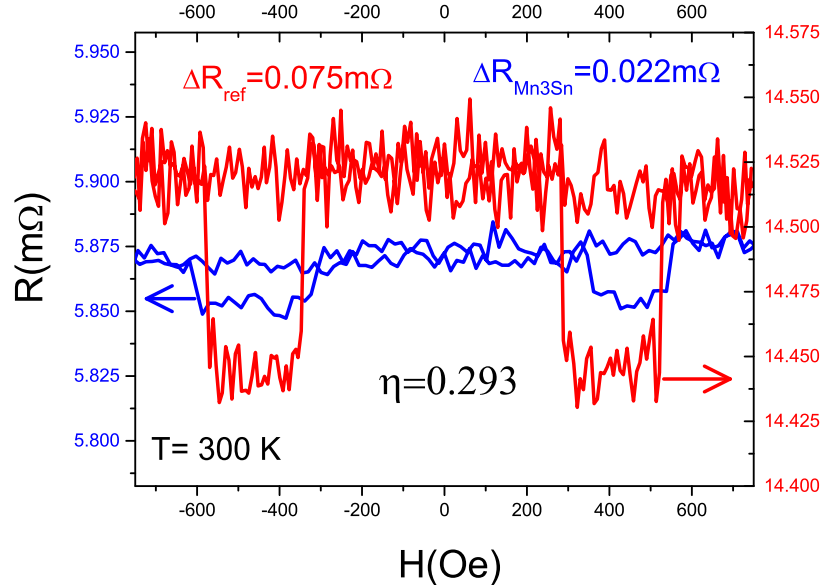


FIG. S8: Nonlocal resistance R_{NL} as a function of magnetic field for reference and spin Hall device measured at room temperature. This measurement was done on the same semiconducting Mn_3Sn nanowire as shown in Fig. S7. We found spin diffusion length $\lambda_S \sim 0.46$ nm in this pair of devices comparable to λ_S of the device reported in the main text.